PAPER

A compact transparent polarization-insensitive metasurface with broadband monostatic and bistatic radar cross-section reduction of millimeter-waves

To cite this article: Xiaoluo He *et al* 2022 *J. Phys. D: Appl. Phys.* **55** 355104

View the article online for updates and enhancements.

IOP ebooks™

Bringing together innovative digital publishing with leading authors from the global scientific community.

Start exploring the collection–download the first chapter of every title for free.

A compact transparent polarization-insensitive metasurface with broadband monostatic and bistatic radar cross-section reduction of millimeter-waves

Xiaoluo He[1] (iD)**, Chu Qi**[1] **and Alex M H Wong**[1,2,*]

[1] Department of Electrical Engineering, City University of Hong Kong, Hong Kong Special Administrative Region of China, People's Republic of China
[2] State Key Laboratory of Terahertz and Millimeter Waves, City University of Hong Kong, Hong Kong Special Administrative Region of China, People's Republic of China

E-mail: alex.mh.wong@cityu.edu.hk

Abstract

This paper proposes an optimized optically transparent metasurface (OTM) which achieves broadband monostatic and bistatic radar cross-section (RCS) reduction with polarization and angle insensitivity. Through employing (a) theoretical formulation involving both monostatic and bistatic RCS and (b) unit cell placement optimization using the particle swarm optimization approach, we achieve monostatic and bistatic RCS reduction over a broad bandwidth with a single-layer, ultra-thin metasurface featuring only two types of unit cells. The proposed metasurface has high optical transparency and electrically small size compared to counterparts with similar performances. Simulation and experimental measurement show that the metasurface achieves more than 10 dB monostatic and bistatic RCS reduction from 18 to 34 GHz, which completely covers the 5G mm-wave spectrum. The proposed optically transparent metasurface can find use in many areas, including mm-wave applications, invisible glass technology, and vehicle windshield systems.

Keywords: optically transparent, bipartite metasurface, RCS reduction

(Some figures may appear in colour only in the online journal)

1. Introduction

The metasurface is an artificial surface composed of meta-atoms with unique electromagnetic properties. Many kinds of metasurfaces have been designed in recent years, such as the dielectric metasurface [1, 2], the gradient metasurface [3–5] and the Huygens' metasurface [6, 7]. With its strong ability of manipulating wavefronts, the metasurface finds broad application prospects in applied electromagnetics, photonics, and antenna gain enhancement [7–10]. Among these applications, radar cross-section (RCS) reduction has a promising application prospect. The RCS of an object generally refers to the area intercepting that amount of power, which is scattered isotropically under a plane wave's irradiation. The effective area of a target is expressed as:

$$\sigma = \frac{4\pi R^2 |E_s|^2}{|E_i|^2}, \tag{1}$$

where E_i and E_s are the electric fields of the incident waves and scattered waves. The incident wave could be equivalent

* Author to whom any correspondence should be addressed.

to the plane wave if the distance R is large enough. The RCS is measured in two ways: in (a) monostatic and (b) bistatic RCS systems. In a monostatic RCS system, the transmitter and receiver are co-located, but in the bistatic RCS system, the aspect angles from the transmitter and receiver to the target are different [11]. As RCS is the main factor in measuring the ability of radar detection [11], achieving monostatic and bistatic RCS reduction plays a significant role in attaining electromagnetic stealth.

The metasurface has been considered an attractive device for RCS reduction in recent years. In particular, two main classes—artificial magnetic conductors (*AMCs*) [12–15] and gradient index metasurfaces (*GIMs*) [16, 17] have received strong consideration. The basic idea behind the operation of an *AMC* RCS reduction surface is to achieve destructive interferences between scattered waves, so that these scattered waves can be redirected away from the radar receiver. The representatives of *AMC* structure for RCS reduction are chessboard-related metasurfaces [15, 18, 19]. However, as the *AMC* structure is susceptible to frequency changes, the proposed design has a limited bandwidth of about 5% [13]. Researchers have explored various methods to resolve this limitation, such as increasing the phase mutation range, using multi-layers and using vias in the unit cell design [20–23]. However, metasurfaces with multi-layers and/or wide phase mutation range generally require complex structures, which lead to fabrication difficulties, especially at mm-wave frequencies and beyond. On the other hand, the *GIM* uses a generalized Snell–Descartes' law to convert an incident wave to surface waves or anomalous reflection, thus resulting in monostatic RCS reduction [16]. However, this method requires a continuous or finely discretized phase profile and complex cell design. In addition, most metasurfaces based on the above two methods are focused on monostatic RCS reduction, but do not provide bistatic RCS reduction. In recent years, some works have explored the bistatic RCS reduction, but an experimental demonstration is yet to be reported [15, 17, 24].

While most metasurfaces are designed on printed circuit board technology and made up of opaque metallic and dielectric material, a class of optically transparent metasurfaces has emerged, fulfilling applications such as shielding windows and screen printing technology. Researchers have designed several kinds of metasurfaces with optical transparency for different applications, including the beam steering [25], near-field focusing [26] and scattering reduction [21, 27–31]. However, most proposed optically transparent metasurfaces for RCS reduction have either narrow working bandwidth [32] or complex structures [28–31]. To achieve a broad bandwidth, multi-layer structures [28, 30, 31], large numbers of unit cells [27, 30, 33, 34] and optimization algorithms of the unit cells distribution [35, 36] are widely used. Multi-layer structures can achieve a stable reflection phase difference between two elements in a broad frequency band [28, 34], while metasurfaces with large numbers of elements can provide better scattering reduction, and thus achieve broadband monostatic RCS reduction [37]. However, a multi-layer structure will decrease its optical transparency, and a large number of elements will inevitably increase the size of the metasurface [21, 27], which

may limit their applications. Besides, as the aspect angles from the transmitter and receiver to the target are unpredictable, the monostatic and bistatic RCS reduction should both be considered [17]. In view of this, a surface that achieves both monostatic and bistatic RCS suppression with a simple structure and high optical transparency can open doors to more applications.

This paper present an optimized metasurface for both monostatic and bistatic RCS reduction. In departure to previous works, we develop our formulation accounting for both monostatic and bistatic RCS from the surface. We then employ a particle swarm optimization (PSO) algorithm to find the placement pattern of metasurface unit cells which optimizes both types of RCS. We design the transparent metasurface in an ITO on glass material system, with a single-layer and ultra-thin structure. The simulations and experimental measurements show that the metasurface can achieve more than 10 dB monostatic and bistatic RCS reduction over the frequency range from 18 to 34 GHz (a 62% bandwidth) and across a wide angle range ($-45° \leqslant \theta \leqslant 45°$). Compared to previously proposed RCS reduction metasurfaces, our metasurface boasts a compact structure, high optical transparency, and a broad working bandwidth for both monostatic and bistatic RCS reduction. Crucially, it covers the mm-wave band deployed in 5G networks around the world [38]. The proposed metasurface architecture can find many applications in transparent mm-wave electromagnetic wave engineering in display mount and windshield systems.

2. Metasurface design

2.1. Design of unit cell

We design our metasurface using the bipartite metasurface structure and scattering interference method. The unit cell is composed of one meta-atom layer, a dielectric substrate and a ground plane, as shown in figure 1(a). In our previous work [7], it has been shown that this simple structure can function as a passive Huygens' source and has advantages of robust operation, low-profile and high efficiency. In essence, the combination of meta-atom and the ground layer supports two modes, and the structure's 'Huygens' properties has been explained by previous works [39, 40]. The meta-atom and ground plane are designed using ITO with a conductivity of 10^7 (S m^{-1}) and a thickness of 200 nm. The substrate used here is an ordinary glass of thickness 1.1 mm, which has a permittivity of 5.5 and a loss tangent of 0.03. $U_x = U_y = 4.9$ mm represents the length and width of the substrate (glass) for a unit cell. The size of patterned ITO of each unit cell is $P_x \times P_y$ where $P_x = P_y$. Since we chose the square pattern as our unit cell, the final metasurface is polarization-insensitive. By varying the size of meta-atom, different reflection phase responses can be achieved. It has been shown two unit cells with $180° \pm 37°$ phase difference can achieve efficient scattering cancellation [18], by providing strong suppression to specular reflection [41]. Therefore we choose two unit cell sizes which maintain a stable phase difference across a wide bandwidth stretching from 18 to 34 GHz. The size of the two unit cells are $P_{x0} = P_{y0} = 1.1$ mm (unit cell '0'), and $P_{x1} = P_{y1} = 2.6$ mm
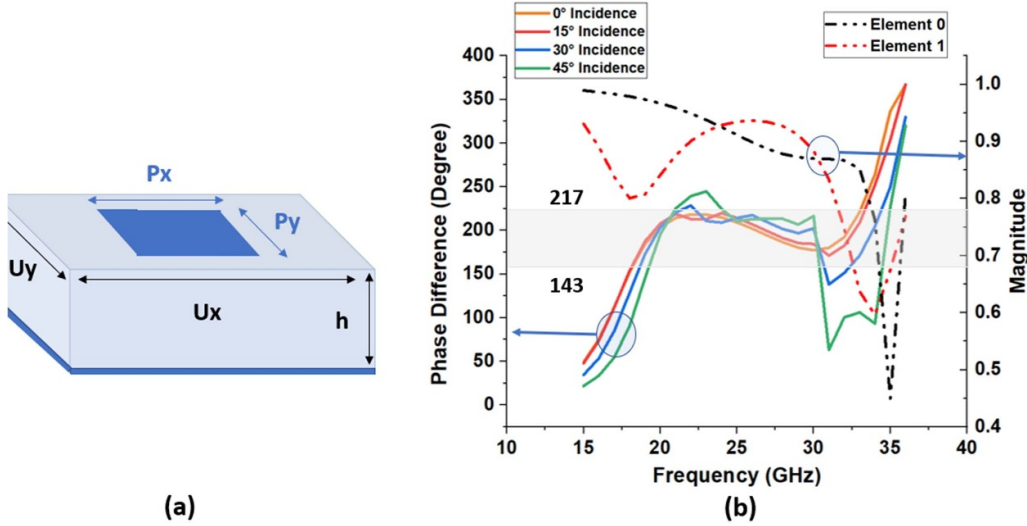
Figure 1. (a) The geometry of the unit cell. (b) The reflection phase difference of two different unit cells under different incident angles (left column), and the reflection amplitude (right column). $P_{x0} = 1.1$ mm (unit cell '0') and $P_{x1} = 2.6$ mm (unit cell '1').

(unit cell '1'). Figure 1(b) shows the simulated reflection phase difference for the chosen two unit cells under different incident angles. It can be observed that when the incident angle is less than 15°, the phase difference is very stable. As the incident angle increases, the phase difference exceeds the set area ($180° \pm 37°$), but the scattering cancellation condition is still met at the center frequency of 26 GHz.

2.2. Optimization and simulation

In this section, we will employ PSO to place into the metasurface the two elements designed in the previous section. We consider the electric field scattered by the metasurface upon normal incidence, which is directly related to the reduction of RCS. From the array theory, the far-field scattering function can be expressed as [42]:

$$F(\theta, \phi) = EP(\theta, \phi) \times AF(\theta, \phi), \tag{2}$$

where $EP(\theta, \phi)$ is the element factor and $AF(\theta, \phi)$ is the array factor. In our design, we only use two similar element patterns but a phase difference of 180°. As is common to the antenna design, the element factor can be ignored as it is a slow-varying function compared with array factor [29, 33, 37, 42]. Thus, the far-field scattering function can be approximately equal to $AF(\theta, \phi)$ and it can be given as [42]:

$$AF(\theta, \phi) = \sum_{m=1}^{M} \sum_{n=1}^{N} \exp\big[j\big[\Phi(m, n) + k\sin\theta[(m - 1/2)U_x\cos\phi$$
$$+ (n - 1/2)U_y\sin\phi]\big]\big], \tag{3}$$

where M and N are the number of elements along the x-axis and y-axis, $\Phi(m, n)$ represents the reflection phase of the element with position index (m, n), ϕ and θ are the azimuth and elevation angles. U_x and U_y represent the center-to-center distance between two adjacent elements along the x-axis and

y-axis. The directivity $\mathrm{Dir}(\theta, \phi)$ of the metasurface can be expressed as [42]:

$$\mathrm{Dir}(\theta, \phi) = \frac{4\pi |AF(\theta, \phi)|^2}{\int_{\phi=0}^{2\pi} \int_{\theta=0}^{\pi/2} |AF(\theta, \phi)|^2 \sin\theta \, d\theta \, d\phi}. \tag{4}$$

Next, we will analyze how the $AF(\theta, \phi)$ affects both monostatic and bistatic RCS reduction. The monostatic RCS reduction, compared to the perfect electric conductor (PEC) surface with the same size, can be expressed as:

$$\mathrm{Mono\text{-}RCS\ (reduction)} = 10\log\left[\frac{\lim_{R\to+\infty}\left(4\pi R^2 \frac{|E_s|^2}{|E_i|^2}\right)}{\lim_{R\to+\infty}\left(4\pi R^2(1)^2\right)}\right]$$
$$= 10\log\left[\frac{|E_s|^2}{|E_i|^2}\right], \tag{5}$$

where R is the distance between the antenna and scatter, and E_i, and E_s represent the incident and scattered electric field in the direction of the radar relative to the scatter. We note that (5) is defined such that a negative value for RCS(reduction) indicates RCS reduction. For example, RCS(reduction) $= -10$ dB means the RCS is reduced 10 dB compared to a PEC of the same size. For a fixed size metasurface with $N^2 (M = N)$ elements, the monostatic RCS reduction under normal incidence can be approximated as:

$$\mathrm{Mono\text{-}RCS(reduction)} = 10\log\left(\frac{AF(\theta, \phi)}{|N^2|}\right)^2. \tag{6}$$

Examining (3) and (6), we find the monostatic RCS vanishes (in the ideal case) if we use the same number of meta-atoms with 0 reflection phase and π reflection phase. This shows that chessboard metasurfaces can achieve effective Mono-RCS reduction [15, 18]. On the other hand, the bistatic RCS reduction compared to the same-sized PEC is defined as [17, 43]:
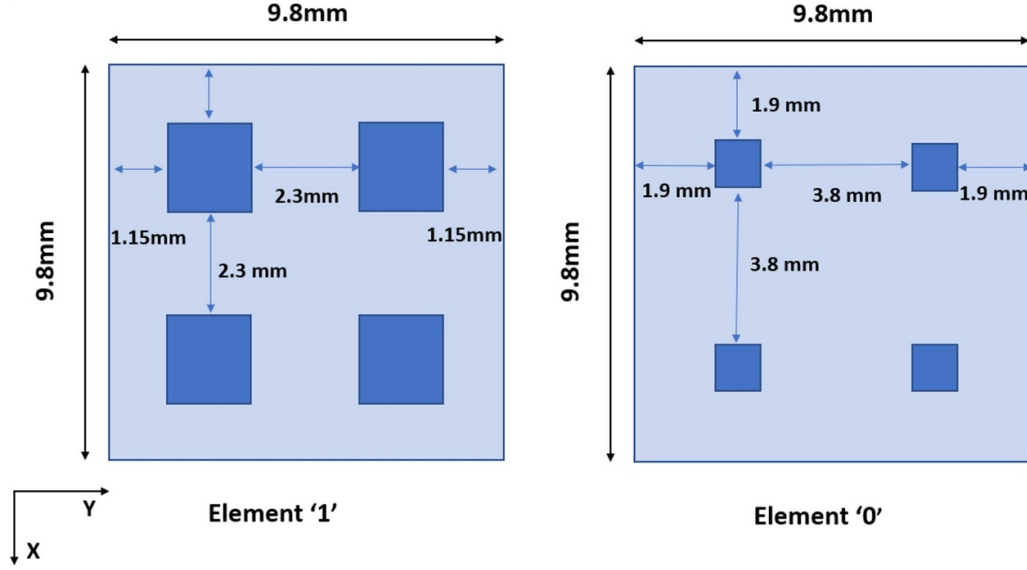
Figure 2. A depiction of the two unit cells. The element size is 9.8 mm × 9.8 mm. Dark blue represents ITO and light blue represents glass.

Bis-RCS(reduction)

$$= 10\log\left[\frac{\max\{\text{Bistatic RCS with metasurface}\}}{\max\{\text{Bistatic RCS with same-sized PEC}\}}\right] \quad (7)$$

the function $\max\{\cdot\}$ covers all elevation and azimuth angles $(0 \leqslant \theta \leqslant \pi/2, 0 \leqslant \phi \leqslant 2\pi)$. Therefore, the bistatic RCS reduction can be expressed as:

$$\text{Bis-RCS(reduction)} = 10\log\left[\frac{\max\{\text{Dir}(\theta,\phi)\}}{\max\{\text{Dir}(\text{PEC})\}}\right] \quad (8)$$

from planar array theory, the maximum directivity of the PEC is given as [42]:

$$\max\{\text{Dir(PEC)}\} = \frac{4\pi A}{\lambda^2}, \quad (9)$$

where λ represents the wavelength and A represents the area of the PEC, which should be equal to the size of the metasurface. For a metasurface with $N^2 (M = N)$ unit cells, each of the lateral size is U^2. So the bistatic RCS reduction can be finally expressed as:

$$\text{Bis-RCS(reduction)} = 10\log\left[\frac{\lambda^2\max\{\text{Dir}(\theta,\phi)\}}{4\pi\,N^2U^2}\right]. \quad (10)$$

This equation is consistent with [37]. It is important to note that a smaller $\max\{\text{Dir}(\theta,\phi)\}$ for all scattering angles means both good monostatic and bistatic RCS reduction.

We now make an observation on the relationship between N, the size of the metasurface, and the extent of bistatic RCS reduction. Cui *et al* [37] established that when the ratio between U and λ is between 0.6 and 3.0, the RCS reduction performance remains nearly invariant. Thus, in this optimal range, the number of elements and the directivity $\max\{\text{Dir}(\theta,\phi)\}$ are the main factors of bistatic RCS reduction. Better RCS reduction can be achieved for a larger number of

N, but a larger N generally means a larger size of the metasurface, which makes fabrication more complicated, increases the cost, and limits the application for the metasurface. Hence we aim to reduce, as much as possible, the number of elements N by optimizing the placement of the two types of unit cells. We achieve this by using the PSO procedure [44] to minimize $\max\{\text{Dir}(\theta,\phi)\}$ at the center frequency, which also minimizes $\max\{\text{AF}(\theta,\phi)\}$. Different from the previous optimized RCS reduction metasurface [35], which only consider the specular reflection of $\max\{\text{Dir}(\theta,\phi)\}$, we are exploring the $\max\{\text{Dir}(\theta,\phi)\}$ for all reflection angles, and thus arrive at the optimized suppression for both monostatic and bistatic RCS, as indicated in (6) and (10). We choose the PSO as it is computationally fast and especially suitable for a large number of particle swarms [44]. We thus use particle swarm to optimize the placement of the two types of unit cells onto the metasurface. To speed up the optimization process, we construct an element by repeating two unit cells along x and y-directions as shown in figure 2. Then each element has four identical unit cells, thus only 10×10 elements need to be optimized, which reduces the optimization vector of 100 elements. More specifically, we encode each possible placement pattern into a 'particle', which is a sequenced vector of 100 elements (each element is either a '1' or a '0'). We set to decide to use a population of 50 particles. These particles are randomly chosen at first, but eventually they converge to the best fitness value by continually comparing their current best solutions. The personal best solution and global best solution are represented by *pbest* and *gbest*, respectively, we continually update their positions (X) and velocities (V) based on the selected best solution. In our design, we use:

$$Fitness = \sum_{m=1}^{N}\sum_{n=1}^{N}\max[Dir], \quad (11)$$

as our fitness function. A larger value of fitness indicates a larger value of $\max\{\text{Dir}(\theta,\phi)\}$, which in turn indicates a stronger
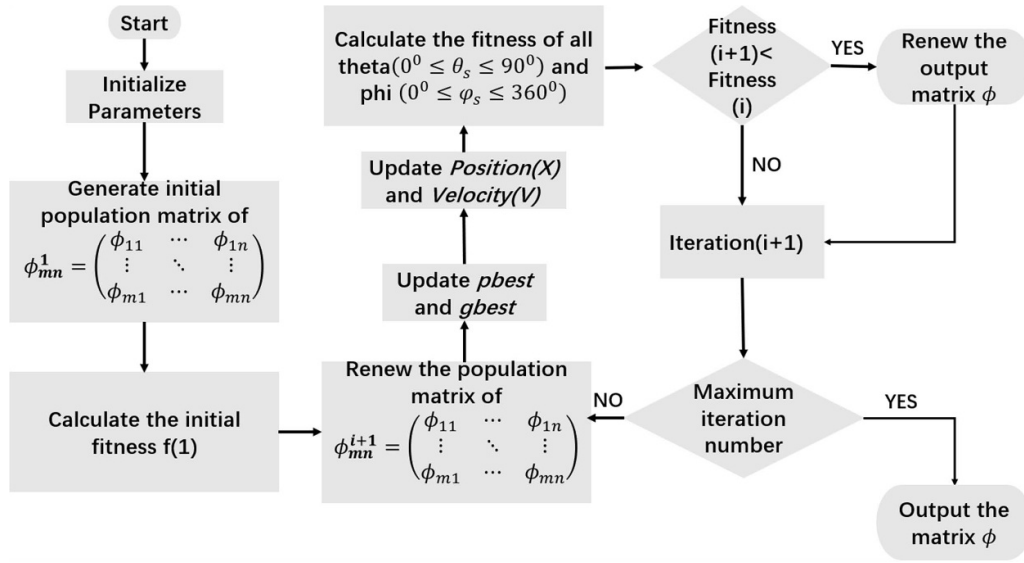
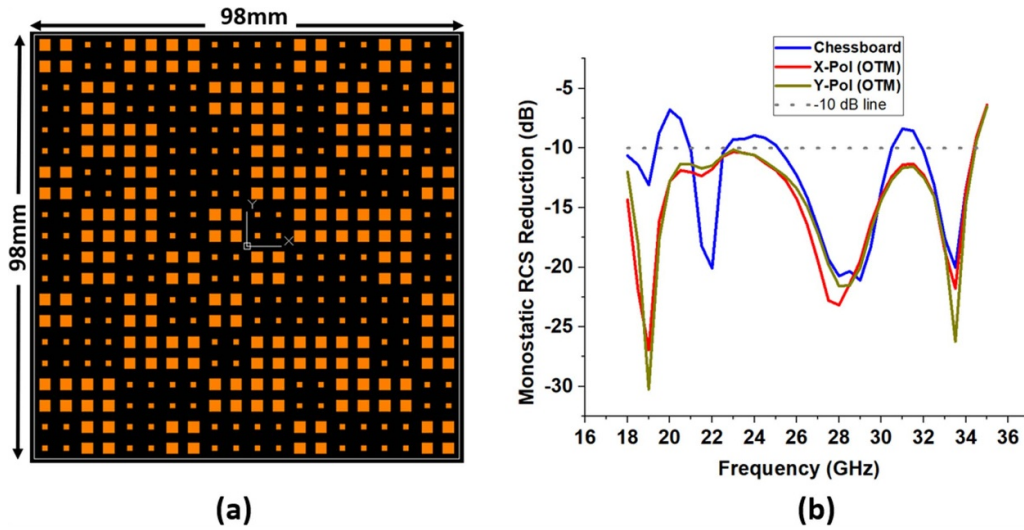**Figure 3.** A flow chart showing the PSO algorithm.

Figure 4. (a) A diagram of the optimized metasurface. (The orange rectangular patterns are ITO meta-atoms.) (b) Simulated monostatic RCS reduction compared to PEC.

RCS from the meatsurface. Thus, we minimize the fitness value to optimize RCS reduction. Figure 3 shows a flowchart describing the optimization procedure.

We set the number of iterations to 1000, which we find sufficient for converging the optimization process. Figure 4(a) shows the optimized metasurface. The metasurface size is 98 mm × 98 mm; the thickness is 1.1 mm. There are in total 400 elements in a square (20 × 20) formation. Figure 4(b) shows the simulated monostatic RCS reduction of the optimized metasurface and the chessboard metasurface compared to the PEC. It shows that a 10 dB RCS reduction is achieved over a broad bandwidth from 18 to 34 GHz for the optimized metasurface, which is a wider bandwidth than that achieved by a chessboard metasurface of the same size. In addition, as we have chosen a symmetrical structure, the RCS of our metasurface is largely polarization insensitive. Slight

deviations in figure 4(b) reflect the level of accuracy in our simulation.

Figure 5 shows 3D scattering patterns of the designed metasurface under normal incidence, compared to the chessboard metasurface and a PEC of the same size, for three different frequencies within the operation bandwidth. The peak scattered amplitude for each pattern is shown on the bottom of the respective sub-plots. From these figures, we see that the bistatic RCS of the optimized metasurface reduced dramatically by 12, 13.5 and 10.7 dB at 20, 26 and 31 GHz respectively. The bandwidth performance exceeds that of the chessboard metasurface, which includes a few pockets within this bandwidth where the RCS is reduced by less than -10 dB.

We also explore the bistatic RCS reduction performance for different directions of incidence (θ_i). Figure 6 shows that

J. Phys. D: Appl. Phys. **55** (2022) 355104

X He *et al*

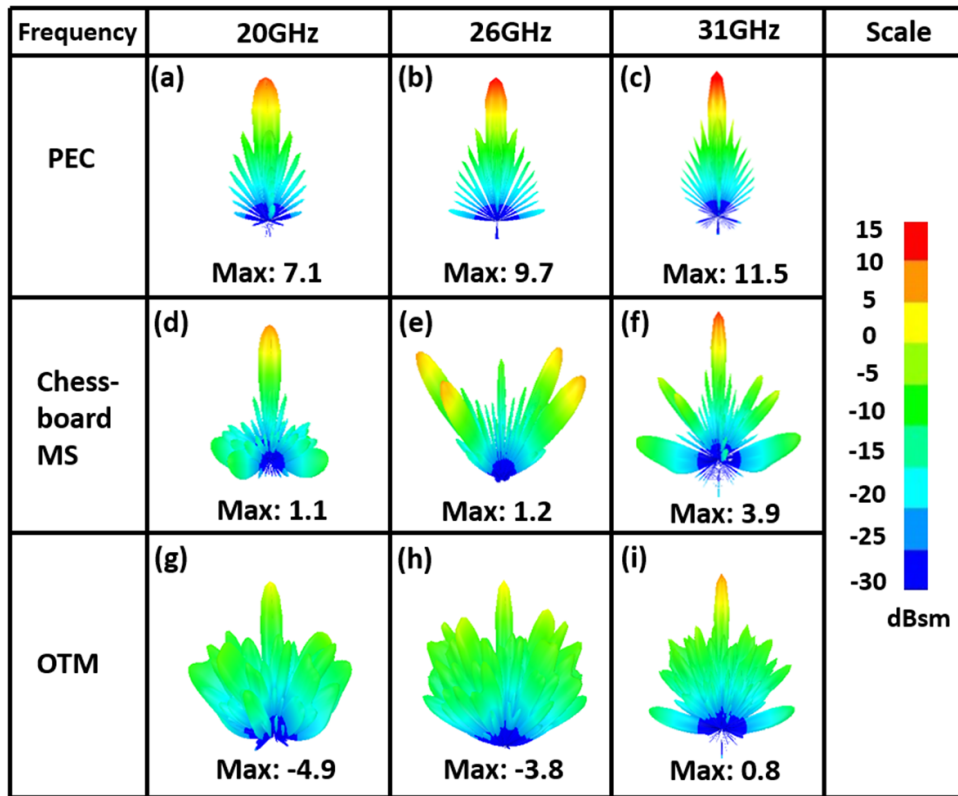| Frequency	20GHz	26GHz	31GHz	Scale
PEC	(a) Max: 7.1	(b) Max: 9.7	(c) Max: 11.5	
Chess-board MS	(d) Max: 1.1	(e) Max: 1.2	(f) Max: 3.9	15 10 5 0 -5 -10 -15 -20 -25 -30 dBsm
OTM	(g) Max: -4.9	(h) Max: -3.8	(i) Max: 0.8	

Figure 5. The 3D back scattering patterns of bistatic RCS under the normal incidence. The comparisons of the reflected scattering electrical field between the PEC, the chessboard metasurface and the OTM under different frequencies.
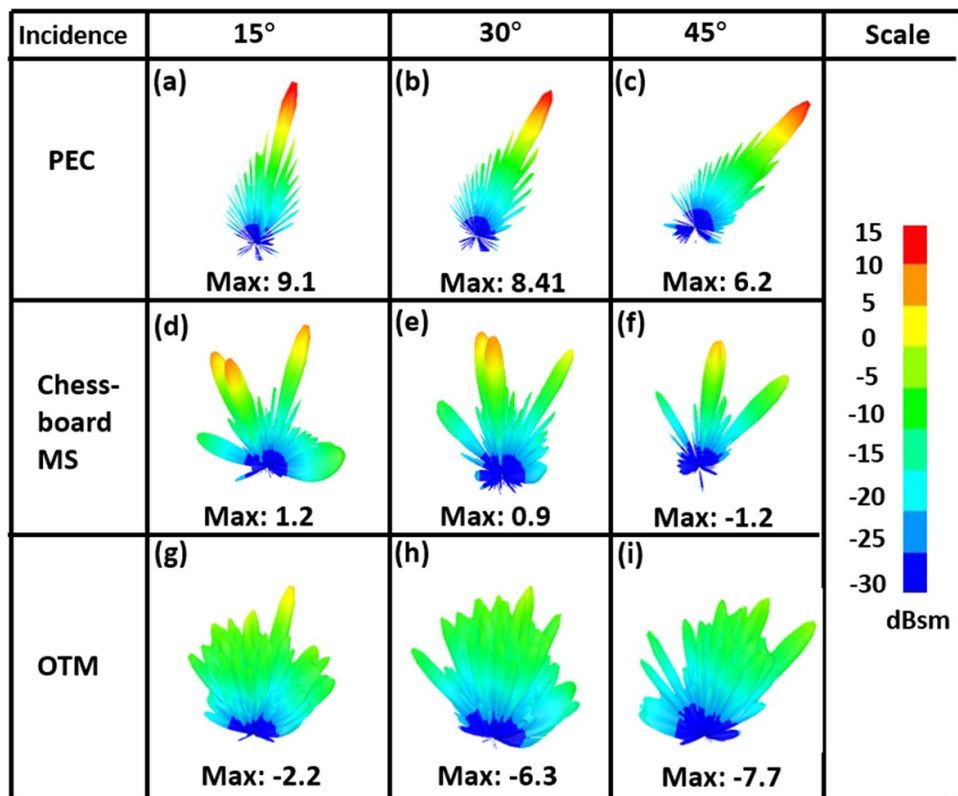
Incidence	15°	30°	45°	Scale
PEC	(a) Max: 9.1	(b) Max: 8.41	(c) Max: 6.2	
Chess-board MS	(d) Max: 1.2	(e) Max: 0.9	(f) Max: -1.2	15 10 5 0 -5 -10 -15 -20 -25 -30 dBsm
OTM	(g) Max: -2.2	(h) Max: -6.3	(i) Max: -7.7	

Figure 6. The 3D back scattering patterns of bistatic RCS under different incidence angles. The comparisons of the reflected scattering electrical field between the PEC, chessboard metasurface and the OTM under 26 GHz.
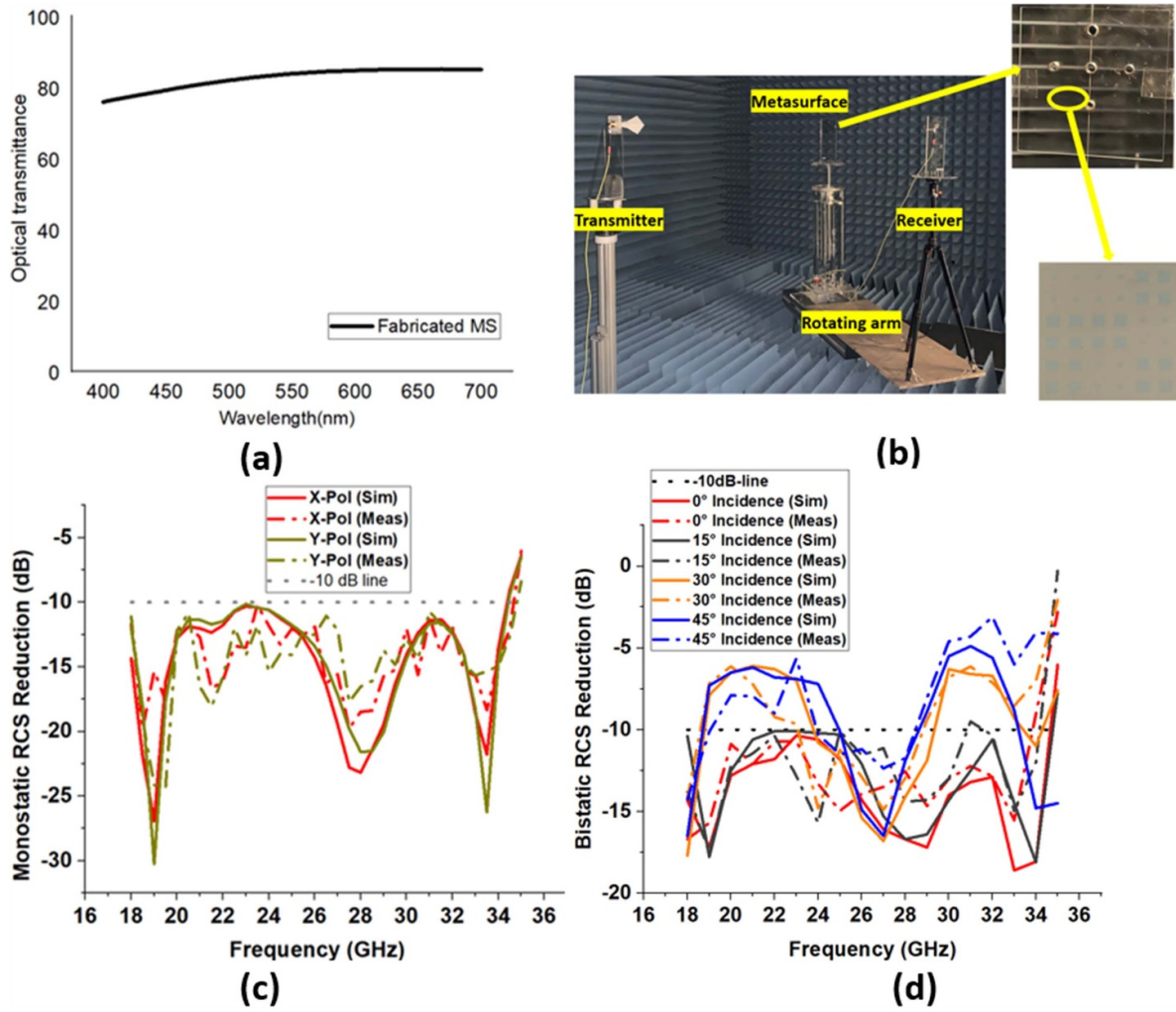
Figure 7. (a) The measured optical transmittance of metasurface. (b) A photo of measurement process. (c) The monostatic RCS reduction when compared to PEC. (d) The bistatic RCS reduction when compared to a metal plate of the same size (Sim: simulated result; Meas: measured result).

dramatic bistatic RCS reduction can be observed in the angular region $-45° \leqslant \theta_i \leqslant 45°$. The bistatic RCS of the optimized metasurface reduced by 13.5 dB, 11.3 dB, 14.7 dB and 13.9 dB, for incident angles of 0°, 15°, 30° and 45°, respectively. In comparison, the chessboard metasurface only reduces the bistatic RCS 8.5, 7.9, 7.5 and 7.4 dB. This shows the capability of our metasurface to reduce the bistatic RCS over a wide variation in the incidence angle, which may prove practically useful in achieving alignment. From these figures, we find that our transparent metasurface can achieve more than 10 dB monostatic and bistatic RCS reduction from 18 to 34 GHz for both monostatic and bistatic RCS, and is more stable in the working frequency range compared to the chessboard metasurface.

3. Experimental demonstration

We proceed to fabricate and characterize the metasurface. Figure 7(a) gives the measured optical transmittance of our fabricated metasurface. We can find the average

optical transmittance to be 84%, which is slightly higher than previously reported optically transparent metasurfaces [27, 28, 33, 34]. The high transparency can be attributed to our use of a single ITO layer and ultra-thin structure. Figure 7(b) shows the measurement setup for both monostatic and bistatic RCS reduction. Two horn antennas are used as the transmitter and receiver. The wooden board is used as a rotating arm to measure the reflection at different angles. For monostatic RCS measurement, both the transmitter and receiver are fixed relative to each other. For the measurement of bistatic RCS reduction, the transmitter is fixed to generate the prescribed incidence angle, and the receiver is rotated along a rail to measure the scattered power with respect to angle. To solve the problem of wave blockage when the two horns overlap, we slightly displace the location of the two horns along the vertical direction. Figure 7(c) shows the monostatic RCS reduction. Figure 7(d) shows the simulated and measured bistatic RCS reduction achieved by the metasurface (compared to a metallic plate of the same size) for different frequencies and incidence angles. We measure the RCS in all directions for both the metasurface and the metal plate. The reflected power at the direction
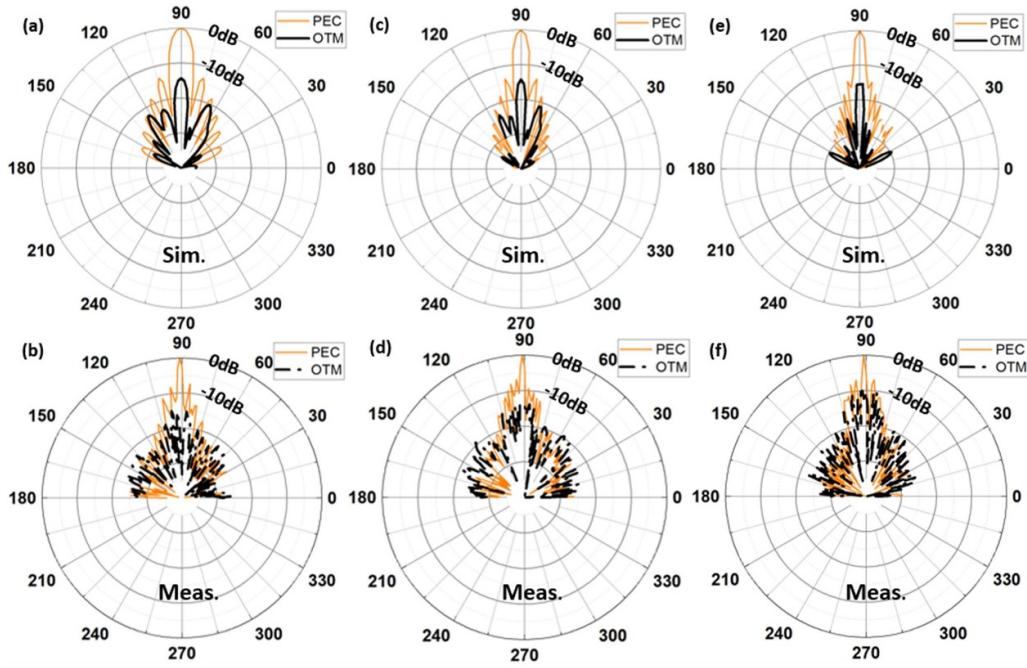
Figure 8. The simulated and measured scattering pattern under normal incidence at the frequencies of (a, b) 18 GHz, (c, d) 26 GHz and (e, f) 34 GHz.
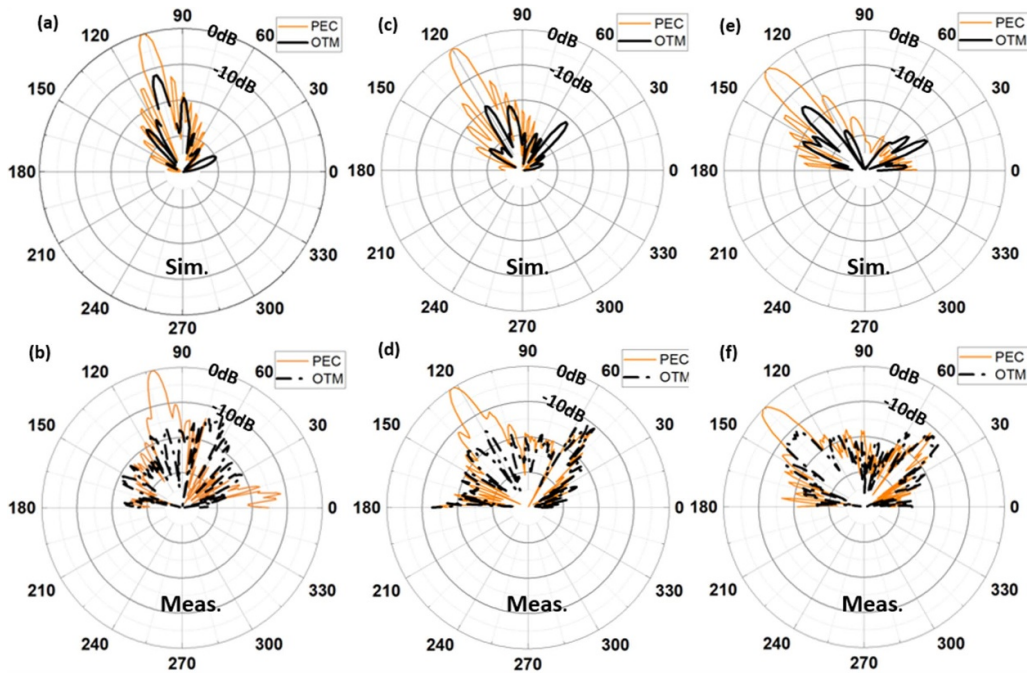

Figure 9. The simulated and measured scattering pattern under the wave incidence of (a, b) 15°, (c, d) 30° and (e, f) 45° at the frequency of 26 GHz.

of strongest scattering from the metasurface is divided (in linear scale) by the reflected power at the direction of strongest scattering from the metal plate (i.e. the specular direction) to obtain the RCS reduction. From the experimental results, more than 10 dB monostatic and bistatic RCS reduction can be achieved by the proposed metasurface from 18 GHz to 34 GHz under normal incidence, which agrees with the full-wave simulation. In addition, the metasurface can maintain −10 dB

bistatic RCS reduction for the whole bandwidth (18–34 GHz) when the incidence angle is below 15°. As the incidence angle increases, the bandwidth will decrease. This is reasonable because the phase difference between the two elements will become unstable. Despite this, within the bandwidth of 25–28 GHz, the metasurface can still achieve more than −10 dB RCS reduction when the incidence increases to 45°. Slight discrepancies between experiment and simulation are attributable to

Table 1. Comparison of the proposed metasurface with other representative works.

Reference	No. of layers	Bandwidth[a]	Full Size[b]	No. of elements	Optical transmittance	Unit cell distribution
[21]	4	7.19–15.26 GHz (MonoR. only: 75%)	$22\lambda \times 22\lambda \times 0.70\lambda$	90 000	75%	Uniform
[24]	1	7.5–13.2 GHz (MonoR.: 60% and BisR.: 55%)	$18\lambda \times 18\lambda \times 0.21\lambda$	1296	No	Chessboard distribution
[27]	3	3.8–6.8 GHz (MonoR. only: 57%)	$63\lambda \times 63\lambda \times 0.53\lambda$	3600	72%	Random
[30]	4	6.3–12.3 GHz (MonoR. only: 90%)	$9.3\lambda \times 9.3\lambda \times 0.22\lambda$	Not given	75%	Uniform
[33]	1	8–14 GHz (MonoR. only: 60%)	$8.8\lambda \times 10.4\lambda \times 0.10\lambda$	1050	80%	Random
Our work	1	18–34 GHz (MonoR. and BisR.: 62%)	$9\lambda \times 9\lambda \times 0.10\lambda$	400	84%	PSO optimized

[a] For the bandwidth column the 10 dB monostatic RCS (MonoR.) and bistatic RCS (BisR.) reductions bandwidth are compared.

[b] λ is the wavelength of central working frequency and size is represented as (length $\times$ width $\times$ height).

etching errors, measurement errors and a possible deviation in the material property of glass, but do not reduce the bandwidth of the metasurface. Figure 8 gives the reflection patterns of normal incidence under different frequencies. In order to further verify the performance of our metasurface at different incident angles, we also give the bistatic RCS reduction for the oblique incidences under 26 GHz, the reflection patterns are plotted in figure 9. We can find the measured results are well consistent with the simulated results. Specifically, the scattering wave has significantly suppressed along the specular direction and redirected to other directions when compared to the PEC.

Table 1 compares the performance of our metasurface with previous representative works. In this table, the bandwidth is defined by the frequency range over which a 10 dB RCS reduction is achieved. The electrical size is referenced to the center wavelength of the metasurface. Compared to the previous optically transparent metasurfaces, our metasurface has the following advantages: single-layer structure, compact size, high optical transmittance, the achievement of wide-angle and broadband RCS reduction for both monostatic and bistatic RCS situations, and stable performance over a wide angular range. Though it does not have the widest operation bandwidth, its 62% bandwidth is respectable and completely covers the 5G mm-wave spectrum. We have achieved comparable bandwidth to [33] which also used a single-layer structure, but leveraging the PSO algorithm, our metasurface is able to achieve this bandwidth for both RCS reduction systems, and with less than half the number of elements as reported in [33]. These advantages potentially open the door to more applications.

4. Conclusion

In this paper, we have reported a broadband, optically transparent RCS reduction Huygens' metasurface built using a compact and optimized structure, on an ITO-on-glass material platform. Simulation and measurements show that our metasurface can achieve more than 10 dB RCS reduction over the frequency range 18–34 GHz. Compared to the aforementioned transparent metasurfaces [25, 32–34], our metasurface boasts (a) stable performance for both monostatic and bistatic RCS reduction (the latter is seldom reported), (b) a very high optical transparency, (c) a sub-wavelength thickness of about $\frac{\lambda}{10}$, (d) a simple and compact structure involving one metalization layer above a ground plane, and (e) a broad working bandwidth (62% from 18 GHz to 34 GHz). Particularly, the mm-wave operation frequency is important for mm-wave applications and relevant to 5G developments worldwide. These advantages make this metasurface an attractive candidate for radar shielding and scattering suppression on display screen and vehicle glass applications.

Data availability statement

The data that support the findings of this study are available upon reasonable request from the authors.

ORCID iD

Xiaoluo He   https://orcid.org/0000-0003-1100-1669

References

[1] Yu Y F, Zhu A Y, Paniagua-Domínguez R, Fu Y H, Luk'yanchukand B and Kuznetsov A I 2015 *Laser Photonics Rev.* **9** 412

[2] Yang Y, Kravchenko I I, Briggs D P and Valentine J 2014 *Nat. Commun.* **5** 5753

[3] Lin D, Fan P, Hasman E and Brongersma M L 2014 *Science* **345** 298

J. Phys. D: Appl. Phys. **55** (2022) 355104

X He *et al*

[4] Zheng G, Mühlenbernd H, Kenney M, Li G, Zentgraf T and Zhang S 2015 *Nat. Nanotechnol.* **10** 308

[5] Zhu H L, Cheung S W, Chung K L and Yuk T I 2013 *IEEE Trans. Antennas Propag.* **61** 4615

[6] Chen M, Kim M, Wong A M H and Eleftheriades G V 2018 *Nanophotonics* **7** 1207

[7] Kim M, Wong A M H and Eleftheriades G V 2014 *Phys. Rev. X* **4** 041042

[8] Khorasaninejad M, Aieta F, Kanhaiya P, Kats M A, Genevet P, Rousso D and Capasso F 2015 *Nano Lett.* **15** 5358

[9] Wong A M H and Eleftheriades G V 2018 *Phys. Rev. X* **8** 011036

[10] Abdo-Sánchez E, Chen M, Epstein A and Eleftheriades G V 2018 *IEEE Trans. Antennas Propag.* **67** 108

[11] Dybdal R B 1987 *Proc. IEEE* **75** 498

[12] Watts C M, Liu X and Padilla W J 2012 *Adv. Mater.* **24** 98

[13] Paquay M, Iriarte J C, Ederra I, Gonzalo R and Maagt P D 2017 *IEEE Trans. Antennas Propag.* **55** 3630

[14] Fu Y, Li Y and Yuan N 2011 *Microw. Opt. Technol. Lett.* **53** 712

[15] Su J, Lu Y, Liu J, Yang Y, Li Z and Song J 2018 *IEEE Trans. Antennas Propag.* **66** 7091

[16] Li Y, Zhang J, Qu S, Wang J, Chen H, Xu Z and Zhang A 2014 *Appl. Phys. Lett.* **104** 221110

[17] Lu Y, Su J, Liu J, Guo Q, Yin H, Li Z and Song J 2019 *IEEE Trans. Antennas Propag.* **67** 4936

[18] Chen W, Balanis C A and Birtcher C R 2015 *IEEE Trans. Antennas Propag.* **63** 2636

[19] Modi A Y, Balanis C A, Birtcher C R and Shaman H N 2017 *IEEE Trans. Antennas Propag.* **65** 5406

[20] Su P, Zhao Y, Jia S, Shi W and Wang H 2016 *Sci. Rep.* **6** 20387

[21] Huang C, Pan W, Ma X and Luo X 2015 *IEEE Antennas Wirel. Propag. Lett.* **14** 1369

[22] Li Y, Zhang J, Qu S, Wang J, Chen H, Xu Z and Zhang A 2014 *Appl. Phys. Lett.* **104** 221110

[23] Samadi F and Sebak A 2021 *IEEE Trans. Antennas Propag.* **69** 1809

[24] Ghayekhloo A, Afsahi M and Orouji A A 2017 *IEEE Trans. Antennas Propag.* **45** 603

[25] Wei Z, Cao Y, Su X, Gong Z, Long Y and Li H 2013 *Opt. Express* **21** 10739

[26] Li L, Zhang P, Cheng F, Chang M and Cui T J 2021 *IEEE Trans. Microw. Theory Tech.* **69** 2015

[27] Meng Z, Tian C, Xu C, Wang J, Li X, Huang S and Qu S 2020 *Opt. Express* **28** 27774

[28] Chen K, Guo W, Ding G, Zhao J, Jiang T and Feng Y 2020 *Opt. Express* **28** 12638

[29] Shen Y, Zhang J, Sui S, Jia Y, Pang Y, Wang J and Qu S 2018 *J. Phys. D: Appl. Phys.* **51** 485301

[30] Xu C, Wang B, Yan M, Pang Y, Wang W and Meng Y 2020 *J. Phys. D: Appl. Phys.* **53** 135109

[31] Huang S, Fan Q, Xu C, Wang B, Wang J, Yang B and Meng Z 2020 *J. Appl. Phys.* **54** 015001

[32] Jing H, Ma Q, Bai G, Bao L, Luo J and Cui T J 2018 *J. Appl. Phys.* **124** 023102

[33] Chen K, Cui L, Feng Y, Zhao J, Jiang T and Zhu B 2017 *Opt. Express* **25** 5571

[34] Zhao J, Zhang C, Cheng Q, Yang J and Cui T J 2018 *Appl. Phys. Lett.* **112** 073504

[35] Khan T, Li J, Chen J, Raza M and Zhang A 2019 *Materials* **12** 3031

[36] Sui S, Ma H, Wang J, Pang Y, Feng M, Xu Z and Qu S 2018 *J. Phys. D: Appl. Phys.* **51** 065603

[37] Cui T J, Qi M Q, Wan X, Zhao J and Cheng Q 2014 *Light: Sci. Appl.* **3** 218

[38] Qualcomm LLC 2020 Global update on spectrum for 4G & 5G (available at: www.qualcomm.com/media/documents/files/spectrum-for-4g-and-5g.pdf)

[39] Anders P and Bozhevolnyi S I 2013 *Opt. Express* **21** 27438–51

[40] Ziolkowski R W 2017 *Phys. Rev. X* **7** 031017

[41] Chen M, Kim M, Wong A M H and Eleftheriades G V 2018 *Nanophotonics* **7** 1207–31

[42] Balanis C A 2016 *Antenna Theory: Analysis and Design* (New York: Wiley)

[43] Edalati A and Sarabandi K 2014 *IEEE Trans. Antennas Propag.* **62** 747

[44] Shi Y 2001 *Proc. 2001 Congress on Evolutionary Computation (IEEE Cat. No.01TH8546)* vol 1 pp 81–86